The Astrophysical Journal Letters, 939:L30 (14pp), 2022 November 10 https://doi.org/10.3847/2041-8213/ac9b10

First Detection of Silicon-bearing Molecules in η Car

C. Bordiu[1], J. R. Rizzo[2,3], F. Bufano[1], G. Quintana-Lacaci[4], C. Buemi[1], P. Leto[1], F. Cavallaro[1], L. Cerrigone[5], A. Ingallinera[1], S. Loru[1], S. Riggi[1], C. Trigilio[1], G. Umana[1], and E. Sciacca[1]
[1] INAF–Osservatorio Astrofisico di Catania, Via Santa Sofia 78, I-95123 Catania, Italy; cristobal.bordiu@inaf.it
[2] Centro de Astrobiología (INTA-CSIC), Ctra. M-108, km. 4, E-28850 Torrejón de Ardoz, Madrid, Spain
[3] ISDEFE, Beatriz de Bobadilla 3, E-28040 Madrid, Spain
[4] Group of Molecular Astrophysics, IFF, CSIC, C/ Serrano 123, E-28006, Madrid, Spain
[5] Joint ALMA Observatory, Alonso de Córdova 3107, Vitacura, 8320000, Santiago, Chile
Received 2022 September 29; revised 2022 October 17; accepted 2022 October 17; published 2022 November 10

Abstract

We present ALMA band 6 observations of the luminous blue variable η Car obtained within the ALMAGAL program. We report SiO $J = 5 \rightarrow 4$, SiS $J = 12 \rightarrow 11$, and SiN $N = 5 \rightarrow 4$ emission in the equatorial region of the Homunculus nebula, constituting the first detection of silicon- and sulfur-bearing molecules in the outskirts of a highly evolved, early-type massive star. The SiO, SiS, and SiN trace a clumpy equatorial ring that surrounds the central binary at a projected distance of $\sim 2''$, delineating the inner rims of the butterfly-shaped dusty region. The formation of silicon-bearing compounds is presumably related to the continuous recycling of dust due to the variable wind regime of η Car, which destroys grains and releases silicon back to the gas phase. We discuss possible formation routes for the observed species, contextualizing them within the current molecular inventory of η Car. We find that the SiO and SiS fractional abundances in localized clumps of the ring, 6.7×10^{-9} and 1.2×10^{-8}, respectively, are exceptionally lower than those measured in C- and O-rich AGB stars and cool supergiants, while the higher SiN abundance, 3.6×10^{-8}, evidences the nitrogen-rich chemistry of the ejecta. These abundances must be regarded as strict upper limits, since the distribution of H_2 in the Homunculus is unknown. In any case, these findings shed new light on the peculiar molecular ecosystem of η Car and establish its surroundings as a new laboratory to investigate the life cycle of silicate dust in extreme astrophysical conditions.

Unified Astronomy Thesaurus concepts: Massive stars (732); Luminous blue variable stars (944); Stellar mass loss (1613); Molecular gas (1073); Dust destruction (2268); Astrochemistry (75); Circumstellar matter (241)

1. Introduction

The massive binary system η Car is composed of an $\sim 100\ M_\odot$ luminous blue variable (LBV) and a hotter, $\sim 30\ M_\odot$ secondary with spectroscopic signatures typical of late-O and W-R stars (Iping et al. 2005). The system is very eccentric ($e = 0.9$), with a well-determined orbital period of 5.54 yr and a minimum separation at periastron of 1.5 au (Damineli 1996; Damineli et al. 2008). The primary, η Car A, is the archetypal member of the LBV family and has captivated astronomers ever since it underwent a violent mass eruption in the 1840s (Frew 2004). This outburst, dubbed the "Great Eruption", released nearly 10^{50} erg (Smith et al. 2003; Smith 2013), rivaling the energetic output of a supernova, and ripped off between 20 and 40 $M_\odot$ of stellar material (Morris et al. 2017). The heavily processed ejecta, ashes of the CNO cycle, formed the Homunculus nebula (Gaviola 1950), a rapidly expanding ($v_{\rm exp} \sim 650$ km s^{-1}; Hillier & Allen 1992; Smith et al. 2018a), hourglass-shaped circumstellar structure with a current-day projected size of $\sim 0.18 \times 0.11$ pc. The Great Eruption was followed, almost 50 yr later, by a second, less energetic outburst (Smith & Frew 2011) that gave birth to an inner structure commonly referred to as the Little Homunculus (Ishibashi et al. 2003), mimicking a gigantic matryoshka doll. The exceptionally complex circumstellar environment produced by these successive events makes of η Car a unique testing ground to investigate (1) the nature of eruptive mass-loss processes in massive stars near the Eddington limit (Smith et al. 2004; Smith & Morse 2019) and (2) the intricate wind interactions in highly massive binary systems (Okazaki et al. 2008; Gull et al. 2009, 2016).

Located 2350 pc from Earth (Smith 2006) toward the near side of the Carina arm, η Car and the Homunculus have been the target of multiple observing campaigns that, spreading across the entire electromagnetic spectrum, allowed for studying the central binary and its surroundings in great detail (see Davidson & Humphreys 2012 for a review). Spectroscopic observations of the circumstellar material have provided an accurate portrait of the atomic gas and dust in and around the Homunculus, unveiling a chemical panorama quite in line with other LBV nebulae, i.e., nitrogen-rich ejecta with a significant oxygen depletion (Davidson et al. 1982, 1986; Dufour et al. 1997; Smith & Morse 2004). However, due to the rather extreme conditions in the outskirts of η Car (hot temperatures, strong far-UV fields), only in the last two decades has the molecular content of the Homunculus begun to draw attention. The first detection of neutral gas was achieved by Smith & Davidson (2001), who reported H_2 $v = 1$ emission at 2.12 μm, tracing the surface of the Homunculus lobes. A few years later, high-velocity absorption lines of CH and OH were identified through UV spectroscopy (Verner et al. 2005), and shortly after, ammonia was reported toward the core region of the Homunculus (Smith et al. 2006). The first molecular survey was carried out by Loinard et al. (2012) with APEX, reporting six new species (CO, CN, HCO^+, HCN, HNC, and N_2H^+) and two isotopologues (^{13}CO and H^{13}CN), thereby confirming η Car as the LBV with the richest molecular inventory.

Initial attempts to map the spatial distribution of this molecular material at high angular resolution with ATCA (HCN; Loinard et al. 2016) and ALMA (CO; Smith et al. 2018b) narrowed down the emission to the central few arcseconds of the Homunculus. The gas, with a velocity dispersion of ∼300 km s^{-1}, has a kinematic age in good agreement with the Great Eruption and follows the distribution of the equatorial structures of warm dust detected in mid-infrared observations (Morris et al. 1999), tracing a sort of equatorial ring or torus of radius ∼4400 au. This ring, disrupted toward the NW—its near side, coincident with the projected direction of the orbit's major axis—delineates the bright rims of the so-called "butterfly" nebula (Chesneau et al. 2005), a region of efficient dust processing where emission from several other species has been resolved, such as HCN and HCO^+ (Bordiu & Rizzo 2019, hereafter BR19). Interestingly, a thorough recalibration of CO ALMA data by Zapata et al. (2022), significantly improving sensitivity, has revealed higher velocity components that may be tracing the walls of the polar lobes of the Homunculus by means of limb brightening.

The most recent observations toward η Car with ALMA and Herschel have continued enlarging its molecular inventory, reporting new detections of H_2O, CH_3OH (Morris et al. 2020), and multiple O-, C-, and N-bearing species and reactive ions (Gull et al. 2020), many of them never detected before in a star of this kind. These findings unravel an unexpected molecular scenario for an early-type high-mass star in its final evolutionary stages. In this work, we analyze ALMA band 6 observations from the ALMAGAL program with a resolution better than ∼0.″4, reporting the first detection of three Si-bearing molecules, namely, SiO, SiS, and SiN, therefore adding yet another piece to the intriguing chemical puzzle of η Car. In Section 2, we describe the observations and data processing methods; in Section 3, we outline the findings of this work, putting them in a broader context and discussing their implications; and in Section 4, we summarize the results and lay out the next steps in this research.

2. Observations and Data Reduction

The ALMAGAL project (PI: S. Molinari) is an ALMA Cycle 7 large program that aims at observing the 1 mm continuum and lines toward more than 1000 dense star-forming clumps with $M > 500\ M_\odot$ and $d < 7.5$ kpc. In the context of this program, the field ID 653755, centered on the coordinates $(\alpha,\ \delta) = (10^h45'03.''27,\ -59°41'03.''74)$, was observed. The field serendipitously covers the position of η Car, located ∼2″ E of the phase center. Observations took place on 2021 April 4, ∼1 yr after the last η Car periastron passage (on 2020.2), using 44 antennas with a maximum baseline of 1.4 km, resulting in a synthesized beam of $0.''38 \times 0.''31$ (P.A.: 1.°38). The field was observed for 45 minutes under good weather conditions (precipitable water vapor ∼2.95 mm).

The spectral setup consisted of four spectral windows, two wide windows covering the frequency ranges 217.00–218.87 and 219.08–220.95 GHz (spectral resolution ∼976.56 KHz) and two narrower, overlapping windows covering the ranges 218.08–218.55 and 220.38–220.85 (spectral resolution ∼244.14 KHz). Raw visibilities were calibrated and imaged employing `CASA` (v6.1.1.15) with ALMA pipeline version 2020.1.0.40. The final products were a 2D continuum map at a reference frequency of 220 GHz and four spectral cubes (one for each spectral window). We manually reprocessed the products using the `SpectralCube`[6] Python library and the `GILDAS/CLASS`[7] software package. Despite the initial continuum subtraction performed on the visibilities before imaging, spectra toward the continuum-emitting region were found to have a highly structured baseline; this issue could be related to the amplification of small calibration systematics by the strong continuum of η Car (Abraham et al. 2022). To deal with this problem, we fitted and subtracted a third-order polynomial to the spectra in all positions. This method was able to remove a significant part of the spurious structure toward the central region while keeping the baseline flat elsewhere. Finally, the data cubes were recentered on the J2000 coordinates of η Car, $(\alpha,\ \delta) = (10^h45'03.''53,\ -59°41'04.''05)$.

In this work, we focus exclusively on the analysis of the cubes with the largest spectral coverage. Throughout the paper, we adopt the following conventions: (1) intensities are expressed in the original flux density scale of janskys per beam, unless explicitly noted otherwise; (2) velocities refer to the local standard of rest (LSR) frame; and (3) positions are given as offsets from the coordinates of η Car.

Table 1
List of Molecules Detected

Species	Transition	E_L (cm^{-1})	ν_0 (GHz)
SiO	$J = 5 \rightarrow 4$	14.48	217.104
SiS	$J = 12 \rightarrow 11$	39.97	217.817
SiN	$N = 5 \rightarrow 4,\ J = 9/2 \rightarrow 7/2$	14.52	218.006
	$N = 5 \rightarrow 4,\ J = 11/2 \rightarrow 9/2$	14.59	218.512
^{13}CN	$N = 2 \rightarrow 1,\ J = 3/2 \rightarrow 1/2$	3.62	217.303
	$N = 2 \rightarrow 1,\ J = 5/2 \rightarrow 3/2$	3.65	217.467
^{13}CO	$J = 2 \rightarrow 1$	3.68	220.398

3. Results and Discussion

3.1. Detections and Identification

After a careful inspection of the cubes, we identified emission from five molecules, namely, SiO, SiS, SiN, ^{13}CO, and ^{13}CN. To our knowledge, this constitutes the first detection of Si- and S-bearing compounds in the outskirts of η Car and, in a wider context, in a highly evolved early-type massive star. Quantum numbers, lower-level energies, and the rest frequencies of the transitions detected are summarized in Table 1.

Silicon is an abundant element (solar abundance $n_{Si}/n_{H2} = 6.47 \times 10^{-5}$; Asplund et al. 2021), most of which is depleted onto dust, being mainly stored in grain cores and, to a lesser extent, in the mantles (Gusdorf et al. 2008). Shocks can destroy dust grains either via ion sputtering or, especially when propagating in a dense medium ($n_{H_2} > 10^4$ cm^{-3}), via grain–grain collisions, effectively releasing Si back to the gas phase (Caselli et al. 1997; Schilke et al. 1997; Guillet et al. 2009, 2011). For this reason, Si-bearing species like SiO are typically regarded as reliable tracers of shocked regions (Martin-Pintado et al. 1992). The SiO and SiS have also been proposed as gas-phase precursors of silicate dust. In the circumstellar envelopes of asymptotic giant branch (AGB) stars, their fractional abundances have been observed to drop at a few stellar radii, possibly due to accretion onto dust grains (Lucas et al. 1992; Schöier et al. 2006, 2007; Wong et al.2016).

[6] https://github.com/radio-astro-tools/spectral-cube
[7] https://www.iram.fr/IRAMFR/GILDAS/

The study of Si-bearing molecules is therefore crucial to understand the life cycle of dust. Both SiO and SiS have been widely searched for in many astrophysical environments; SiO has been detected in molecular clouds (Wilson et al. 1971), envelopes of evolved stars of all chemical types (e.g., Morris et al. 1979; Bujarrabal et al. 1994; Schöier et al. 2006), star-forming regions (Lefloch et al. 1998; Jiménez-Serra et al. 2004), and even in the disk of the B[e] supergiant CPD-52 9243 (Kraus et al. 2015). Likewise, SiS has also been found in circumstellar envelopes of all chemical types (Grasshoff et al. 1981; Schöier et al. 2007; Danilovich et al. 2019; Massalkhi et al. 2019, 2020), star-forming regions with outflows (Dickinson & Kuiper 1981; Ziurys 1988), and, exceptionally, in L1157, a shocked region associated with a Sun-like protostar (Podio et al. 2017). However, no detections have been achieved to date in the outskirts of a highly evolved, early-type massive star like η Car, where the physical conditions are, in principle, much less hospitable.

Contrary to SiO and SiS, SiN is a rather elusive molecule that to date has only been found in three astrophysical environments: the C-rich envelope of IRC+10216 (Turner 1992), the hot molecular core SgrB2(M) (Schilke et al. 2003), and the S-type AGB star W Aql (De Beck & Olofsson 2020).

Our line identification relies upon strong kinematic arguments, as only the SiO, SiS, and SiN transitions listed in Table 1 match the observed velocities of CO, HCN, and HCO^+ (BR19). Still, we assessed other alternative identifications to account for the complex kinematics of the circumstellar material. Several transitions of CH_3OH and SO_2 lie within 100 MHz of the rest frequencies of SiO and SiS (217.104 and 217.817 GHz, respectively). However, we find their corresponding velocities to be largely incompatible with those of CO, HCN, and HCO^+, in some cases off by more than $\sim$100 km s^{-1}. Moreover, the CH_3OH and SO_2 transitions have lower-level energies (E_L) in the range of $\sim$500–2000 cm^{-1}, much higher than SiO and SiS, as well as the methanol transition detected by Morris et al. (2020). The excitation conditions required by such transitions are only achievable very close to the binary, where vibrationally excited HCN has been reported (BR19).

Similarly, we searched for other candidate lines to explain the features at 218.006 and 218.512 GHz that we attribute to SiN. Both SiN components lie close in frequency to the $10_{0,10} \rightarrow 9_{0,9}$ and $9_{2,7} \rightarrow 8_{2,6}$ transitions of $^{29}SiC_2$ at 218.011 and 218.506 GHz. However, the nondetection of the $10_{0,10} \rightarrow 9_{0,9}$ transition of the presumably more abundant isotopologue SiC_2 at 220.773 GHz makes this identification highly unlikely, leaving SiN as the only plausible option.

3.2. Spatial Distribution and Kinematics

All of the molecules trace a clumpy "C-shaped" structure, following the overall spatial distribution of the equatorial ring already seen in CO, HCN, $H^{13}CN$, and HCO^+ (see Figure 1 in BR19). No molecular emission is detected in the direction of the star. Figure 1 shows the peak intensity maps of SiO and ^{13}CO, the brightest lines in each band, divided by the corresponding rms maps. The resulting signal-to-noise ratio (S/N) maps highlight the genuine line emission while removing spurious features toward the continuum-emitting region—where the noise is higher—that affected the original peak intensity maps. For convenience, we identified 12 significant emission clumps above 5σ in the SiO map. The clumps were labeled from A to L counterclockwise starting from the N, as indicated in Figure 1, and will henceforth serve as a positional reference.

The SiO clumps have an average projected distance to the star of $\sim$2″. Despite their similar distribution along the butterfly region, SiO and ^{13}CO are not perfectly correlated; closer inspection reveals an offset between emission peaks, especially pronounced in the SE/E clumps (the far side of the ring), the SiO being closer to η Car in projection by $\sim$0.″1–.″0.2 ($\sim$275–550 au). This offset, smaller than the beam, is genuine and was validated by checking against the CO $J = 3 \rightarrow 2$ data presented in BR19. It suggests that SiO may preferentially trace the inner rims of the butterfly nebula, more exposed to the fast wind of η Car, as proposed by Chesneau et al. (2005).

The spatial distribution of the other Si-bearing compounds is even more patchy, with reliable detections only in a subset of the clumps. The SiS is detected toward clumps C, D, E, F, G, H, J, and L, whereas SiN is only found in positions D, F, G, and H. In clump F, the two transitions at 218.006 and 218.512 GHz are detected at an $\sim 3\sigma$ level, whereas in the other clumps, only the 218.512 GHz component is unambiguously found. Since the two transitions are expected to have similar line strengths, a relative difference could be explained by either noise fluctuations or very localized non-LTE effects (as observed in NH_3 around G79.29+0.46; Rizzo et al. 2014).

In any case, the low S/N of most of these detections prevents us from producing meaningful maps of SiS and SiN, as the lines are only clearly resolved in averaged spectra. In this sense, the nondetection of SiS and SiN in clumps where SiO is present may either be a matter of sensitivity or imply an actual chemical differentiation. Likewise, the overall clumpiness of Si-bearing species may be due to the limited sensitivity of the data or indicate that only in certain places are the right physical conditions for their formation met in the presence of sufficient Si. In view of the different relative intensities and radial offset between SiO and ^{13}CO, we are inclined to favor the second scenario.

The insets in Figure 1 show the spectra of SiO and ^{13}CO, averaged in a circular aperture of radius 2.″5 centered on the star, that encompasses the main emission features. The two molecules show a similar overall profile, with most of the emission originating from the velocity range (−100, +100) km s^{-1}. We performed a Gaussian fitting, identifying three major kinematic components that explain the overall motion of the gas: blueshifted material toward the W/NW, the near side of the ring; redshifted gas toward the S/SE, the far side; and material toward the NE and SW moving at velocities relatively close to the systemic velocity of η Car (−19.7 km s^{-1}; Smith 2004). However, we note that the relative intensities of the components differ between SiO and ^{13}CO. In SiO, the redshifted component is the strongest, as clumps on the far side (e.g., E, F, and G) are significantly brighter than the others. Such a difference may be a consequence of local density enhancements or modulations intrinsic to the orbital phase.

Individual clumps, on the other hand, exhibit a more complex kinematic structure, with multiple velocity components spreading over several tens of kilometers per second. This dispersion is more significant in the clumps located S of the star, possibly tracing turbulent or stratified gas. For the subsequent analysis, beam-averaged spectra were extracted in all 12 positions. Full spectra are presented in Appendix A. Figure 2 shows the spectra of clump F, the brightest one in SiO,

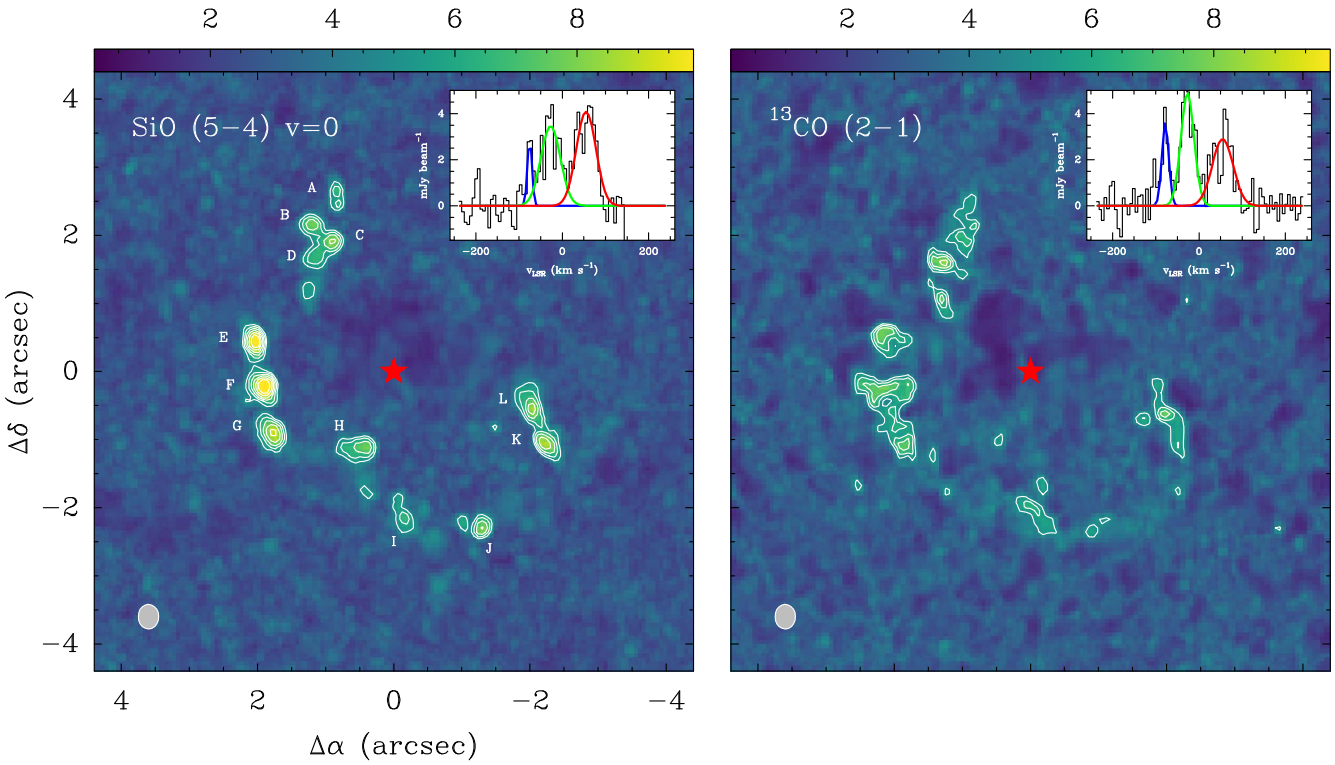

Figure 1. The S/N maps of SiO $J = 5 \rightarrow 4$ ($v = 0$) and ^{13}CO $J = 2 \rightarrow 1$ toward η Car. Contours are from 5 to 10. The position of η Car is indicated by the red marker. The approximate beam size is shown in the bottom left corner. The insets show the average spectrum of each molecule, computed in a region of radius 2.″5. The dominant kinematic components are highlighted with Gaussian profiles. Since SiO appears next to the edge of the band, its spectrum is truncated above 140 km s^{-1}.

as a representative example, while Figure 3 presents a closer view of the spectra of the Si-bearing molecules in that position, aligned in velocity.

3.3. Column Densities

We employed the software MADCUBA[8] (Martín et al. 2019) to determine the column densities and molecular abundances of the observed species in all clumps. MADCUBA estimates the physical parameters of the emission by comparing the observed spectra with synthetic models computed under the only assumption of local thermodynamic equilibrium (LTE). The AUTOFIT function of the MADCUBA package Spectral Line Identification and Modeling performs a nonlinear least-squares fit to the observed spectra following the Levenberg–Marquardt algorithm (Levenberg 1944; Marquardt 1963) and returns the set of parameters (column density N, excitation temperature T_{ex}, line velocity, and FWHM) that best reproduces the observed line profiles.

For the calculations, the spectra were rescaled to a main-beam temperature (T_{mb}) scale using

$$T_{mb} = 1.222 \times 10^6 \frac{S_\nu}{\nu^2 \theta_{maj} \theta_{min}}, \quad (1)$$

with S_ν the flux density in janskys per beam, ν the reference frequency in gigahertz, and θ_{maj} and θ_{min} the major and minor axes of the beam in arcseconds.

With just a single rotational transition observed in all of the lines, the excitation temperature cannot be determined. We thus have proceeded under the assumption of thermal coupling between dust and gas, setting the T_{ex} of the clumps to the blackbody equilibrium temperature of the dust grains, as given by Smith et al. (2003),

$$T_{BB} = 13,100\, R_{AU}^{-1/2}\ \mathrm{K}, \quad (2)$$

where R_{AU} is the physical distance from each clump to η Car in astronomical units, deprojected assuming an inclination of 41° (Smith 2006). This approach yields temperatures in the range 150–200 K, similar to those typically assumed in the literature. Finally, since all of the clumps have a size comparable to the beam, we did not apply any filling factor correction.

Table 2 presents the column densities of SiO, SiS, SiN, ^{13}CO, and ^{13}CN in the clumps with their associated uncertainties. When a molecule is not detected, the 3σ upper limit of the column density is provided. As discussed in Section 3.2, some clumps show a complex kinematic structure, which results in multiple resolved velocity components. For those, the sum of independent column densities along the line of sight is provided. Line fitting parameters (observed velocity v, FWHM Δv, and integrated intensity) for all of the components with an S/N above 3σ are listed in Appendix B.

We also checked for non-LTE effects using RADEX (van der Tak et al. 2007). RADEX solves the statistical equilibrium equations using the escape probability formulation (Sobolev 1960) without assuming LTE conditions. For the calculation, we set the H_2 volume density to 10^8 cm^{-3}, as suggested by Gull et al. (2020); the kinetic temperature to the temperatures in Table 2; and the column density to the values provided by MADCUBA for each component. Then, we compared the integrated line intensities observed with those predicted by RADEX. We found an average agreement of better than 85% for SiO, better than 95% for SiS, and better than 97% for ^{13}CO.

[8] MAdrid Data CUBe Analysis (MADCUBA), developed at the Centro de Astrobiología; https://cab.inta-csic.es/madcuba/.

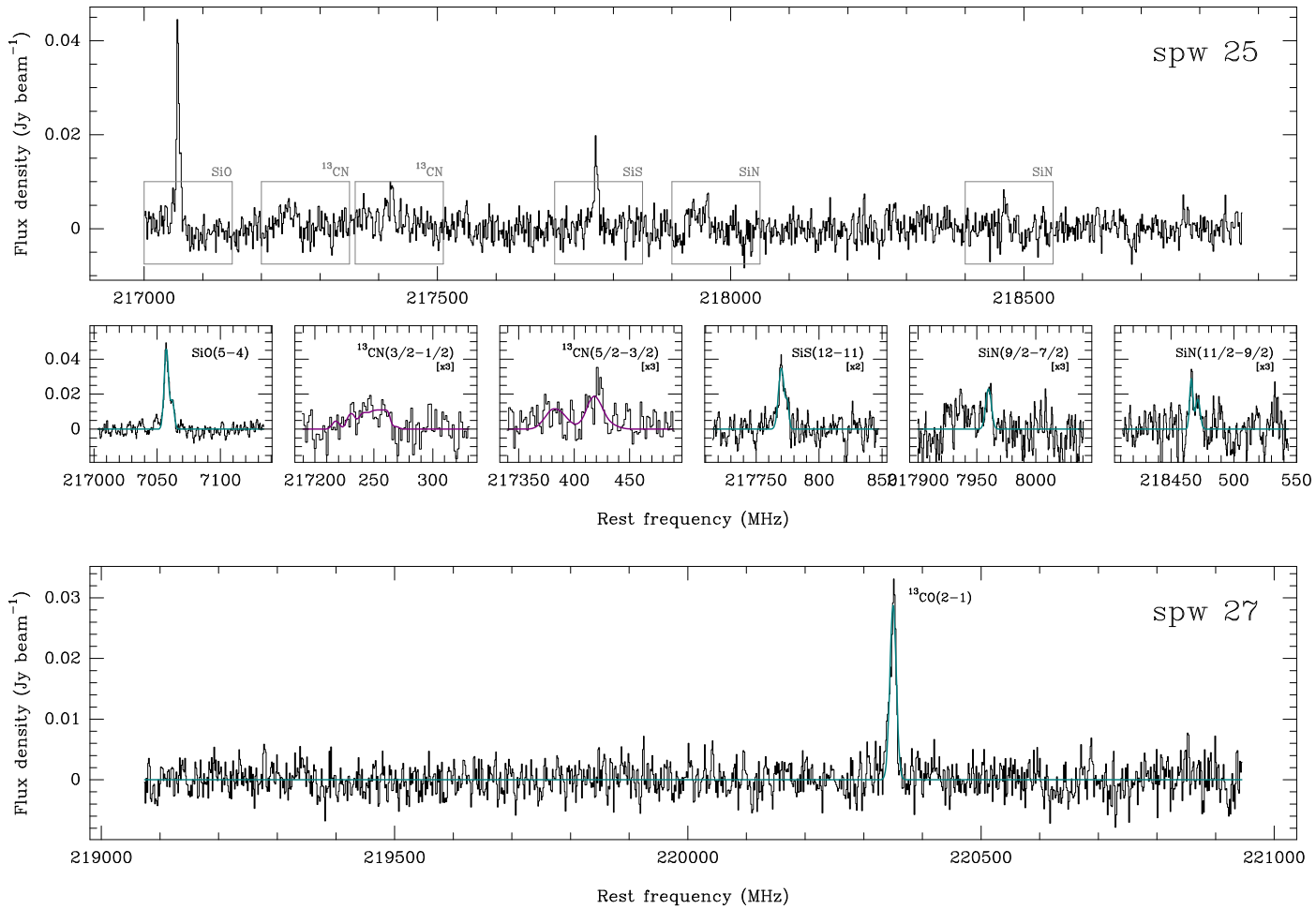

Figure 2. Beam-averaged spectra of clump F. Top panel: full band from 217.0 to 218.8 GHz, rebinned to a resolution of 2 km s^{-1}. The insets show zoom-ins of the transitions detected (gray boxes on the full spectrum) at the original resolution, with a Gaussian (blue) or hyperfine (purple) fitting superimposed. The ^{13}CN spectra have been smoothed to better highlight the hyperfine structure. All of the insets have the same flux density scale, with the different lines scaled appropriately for better visibility. Bottom panel: same as the top panel from 219.1 to 221.0 GHz.

The slight discrepancy in SiO could perhaps be attributed to a possible weak maser contribution (see Section 3.6). In any case, considering the assumptions made, we conclude that non-LTE effects, while present, might not be particularly significant for the measured transitions.

All of the lines are found to be optically thin, with τ in the range (0.01–0.1). When detected, the column densities range roughly from 0.7 to 3.5×10^{14} cm^{-2} for SiO, 1.3 to 7.1×10^{14} cm^{-2} for SiS, and 0.7 to 1.7×10^{15} cm^{-2} for SiN. We observe column density variations among clumps up to a factor of $\sim$5 in the case of SiO and SiS. Considering only the positions where the two species are detected (C, D, E, F, G, H, J, and L), the [SiO/SiS] ratio has an average value of 0.6, meaning a slight overabundance of SiS over SiO. The clumps where SiS is not detected, namely, A, B, I, and K, have much higher ratios when considering the N(SiS) upper limits. Since the rms is similar across the clumps, the strong detections of SiO in the absence of SiS in these positions may indicate a chemical differentiation. It is noteworthy that these clumps are among those located farthest from the star and hence with the lowest T_{ex}. Contrarily, SiN is detected only toward four clumps (one of which is a tentative detection; see Table 3), showing the highest column density of the Si-bearing species. These clumps are not among those with the highest SiO and SiS column densities, which could possibly imply a localized overabundance of SiN.

3.4. Molecular Abundances

Translating column densities into molecular abundances is not straightforward in η Car, as the distribution of H_2 at angular scales comparable to the clumps is unknown. We are thus forced to adopt the global value of $N(H_2) = 3.0 \times 10^{22}$ cm^{-2} determined by Smith (2006). Taking average column densities for each molecule, considering only clumps with detections above 3σ, we derive $[SiO/H_2] = 6.7 \times 10^{-9}$, $[SiS/H_2] = 1.2 \times 10^{-8}$, and $[SiN/H_2] = 3.6 \times 10^{-8}$. These values have to be regarded as peak abundances or upper limits, as we are assuming a homogeneous distribution of H_2, which may not reflect reality; i.e., it is likely that H_2 is somewhat enhanced in the clumps, resulting in lower abundances. Nevertheless, these values are a useful first estimate that allows us to put η Car in context with other evolved stars with a rich silicon chemistry.

Figure 4 compares the SiO and SiS abundances of η Car with those measured in other sources, namely, C-rich stars (Massalkhi et al. 2019), O-rich stars (Massalkhi et al. 2020), S-type stars (Ramstedt et al. 2009; Danilovich et al. 2018; De Beck & Olofsson 2020), the red supergiants VY CMa (Ziurys et al. 2007) and NML Cyg (Singh et al. 2021), and the yellow

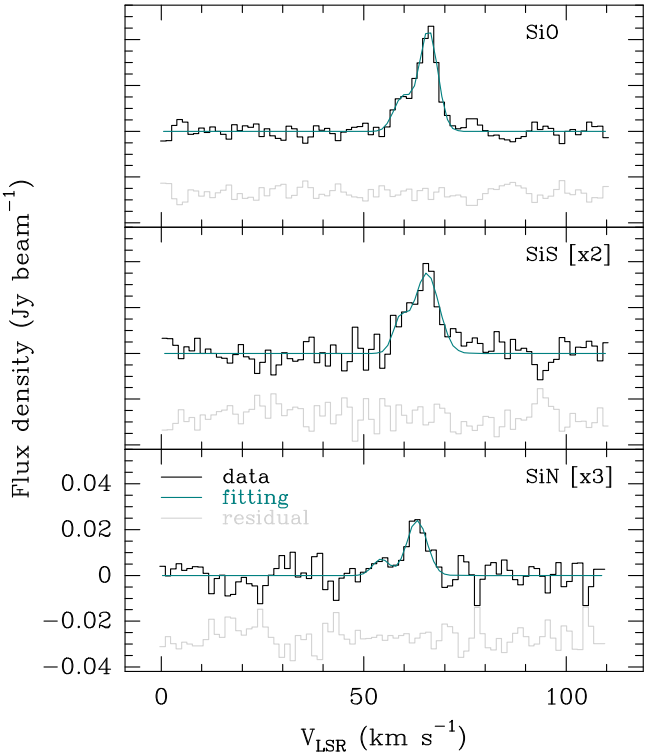

Figure 3. Velocity-aligned spectra of the Si-bearing molecules detected in clump F. The SiN transitions at 218.006 and 218.512 GHz have been stacked to improve S/N. For each spectrum, a Gaussian fitting (blue) and the corresponding residual (gray) are shown. The relative scaling of the lines is the same as in Figure 2.

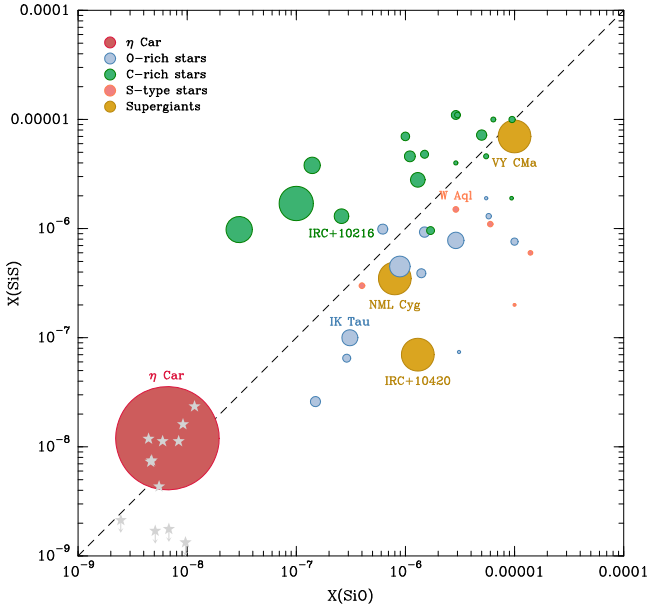

Figure 4. Comparison of abundances of SiO and SiS measured in η Car (this work) and other star types with confirmed detections of the two species: C-rich stars (Massalkhi et al. 2019), O-rich stars (Massalkhi et al. 2020), S-type stars (Ramstedt et al. 2009; Danilovich et al. 2018; De Beck & Olofsson 2020), the yellow hypergiant IRC+10420 (Quintana-Lacaci et al. 2016), and the red supergiants VY CMa (Ziurys et al. 2007) and NML Cyg (Singh et al. 2021). Some relevant objects have been labeled for clarity. The size of the markers is proportional to the square root of $\dot{M}$. The gray stars around η Car indicate the abundances of individual clumps. The dashed line represents [SiO/SiS] = 1.

hypergiant IRC+10420 (Quintana-Lacaci et al. 2016). Only stars with confirmed detections of the two species have been included. We find that the abundances of η Car are exceptionally low, more than 1 order of magnitude lower than in other sources. This is in excellent agreement with the trend observed by González Delgado et al. (2003), who surveyed a large sample of AGB stars and found that the SiO fractional abundance and mass-loss rate were inversely correlated regardless of the chemical type of the envelope, possibly as a consequence of enhanced depletion of SiO onto dust grains at higher densities. The case of SiS is particularly interesting. It is not detected in envelopes with $\dot{M} < 10^{-6}\ M_{\odot}\ \mathrm{yr}^{-1}$, possibly due to a lack of available Si and S. Above this threshold, Massalkhi et al. (2019, 2020) found weak hints of an abundance decrease with increasing $\dot{M}$ similar to SiO but only in C-rich envelopes. However, the abundances of η Car, with its extreme mass-loss rate of $10^{-3}\ M_{\odot}\ \mathrm{yr}^{-1}$ (Hillier et al. 2001), and other sources with mass-loss rates of a few $\sim 10^{-4}\ M_{\odot}\ \mathrm{yr}^{-1}$, such as NML Cyg and IRC+10420, seem to support this trend. The only exception is VY CMa, which presents large abundances of SiO and SiS despite having a high mass-loss rate ($[\mathrm{SiO/H_2}] = 10^{-5}$, $[\mathrm{SiS/H_2}] = 7 \times 10^{-6}$; Ziurys et al. 2007).

Besides, in η Car, the clumps with detection of SiO and SiS have [SiO/SiS] < 1 (except for clump L), meaning that their silicon chemistry is somewhat closer to that of C-rich stars, where SiS tends to be more abundant than SiO by a factor of a few. Such an abundance ratio is not immediately explainable, considering (1) the composition of the ejecta around η Car, which is rich in N but C- and O-poor, and (2) the lack of reported observations of sulfur-bearing species to explain the formation of SiS (see Section 3.5). In this respect, Zanchet et al. (2018) developed a simple shock model that predicts a slower postshock formation of SiS than SiO and with lower abundances. Still, we emphasize that η Car is an exceptional environment with rather unusual physical conditions that probably will require the development of specific models to properly describe its molecular chemistry. In this context, a way to explain the prevalence of SiS over SiO follows the arguments presented by Massalkhi et al. (2019), who regarded SiS as a more efficient gas-phase reservoir of Si, to the detriment of SiO, which is more easily incorporated back onto dust grains as the density and mass-loss rate increase. Indeed, condensation of SiO—and, to a lesser extent, SiS—onto dust could be a recurring process in the molecular ring. The material in the inner rims of the butterfly region would be constantly recycled, with shocks caused by the binary winds periodically destroying dust and leading to the formation of Si-bearing species. A fraction of these molecules would eventually deplete back to dust in a cycle modulated by the orbital period of 5.54 yr.

Finally, it is worth noting that photodissociation could also play an important role in explaining the observed abundances. Unfortunately, its impact is difficult to calibrate. First, the UV flux to which the circumstellar material is exposed is, again, a function of the orbital phase; depending on the epoch, a large fraction of the ionizing flux from the hotter secondary is blocked by the optically thick primary wind (Gull et al. 2016). Second, the photodissociation rate of SiS is not yet well determined and is usually assumed to be similar to that of SiO (Massalkhi et al. 2019).

Table 2
Column Densities of SiO, SiS, SiN, ^{13}CO, and ^{13}CN in the Positions Indicated in Figure 1

Pos.	($\Delta\alpha$, $\Delta\delta$)	T_{ex} (K)	N(SiO) ($\times10^{14}$ cm^{-2})	N(SiS) ($\times10^{14}$ cm^{-2})	N(SiN) ($\times10^{14}$ cm^{-2})	N(^{13}CO) ($\times10^{17}$ cm^{-2})	N(^{13}CN) ($\times10^{15}$ cm^{-2})
A	(+0.9, +2.6)	154	0.74 (0.07)	<0.64	<1.46	0.69 (0.07)	<0.14
B	(+1.2, +2.2)	166	1.53 (0.21)	<0.51	<1.51	1.19 (0.61)	<0.15
C	(+0.9, +1.9)	180	1.42 (0.11)	2.25 (0.12)	<1.65	1.34 (0.13)	<0.42
D	(+1.2, +1.7)	185	1.39 (0.08)	2.19 (0.26)	7.11 (6.89)	2.61 (0.09)	0.88 (0.15)
E	(+2.0, +0.4)	179	1.79 (0.05)	3.38 (0.41)	<1.62	1.76 (0.10)	0.73 (0.15)
F	(+2.0, −0.2)	173	2.75 (0.24)	4.83 (0.85)	17.38 (7.85)	2.44 (0.19)	0.92 (0.15)
G	(+1.8, −0.9)	163	2.51 (0.50)	3.38 (0.24)	7.46 (0.85)	1.74 (0.46)	<0.42
H	(+0.5, −1.1)	211	3.51 (0.39)	7.05 (1.30)	<2.69	2.89 (0.25)	1.17 (0.34)
I	(−0.3, −2.2)	165	2.90 (0.33)	<0.40	<1.58	3.45 (0.32)	<0.25
J	(−1.3, −2.3)	162	1.33 (0.07)	3.56 (0.36)	<1.54	3.19 (0.15)	<0.17
K	(−2.3, −1.1)	168	2.04 (0.16)	<0.53	<2.02	2.40 (0.15)	1.34 (0.20)
L	(−2.0, −0.5)	180	1.66 (0.07)	1.30 (0.20)	<2.20	2.25 (0.10)	1.34 (0.24)

Note. For clumps with multiple velocity components (see Tables 3 and 4), we provide the sum of the column densities of individual components. When a line is not detected, we provide the 3σ upper limit of the column density.

3.5. Chemistry of Si-bearing Molecules in the Homunculus

The physics of dust formation in the massive winds and eruptions of hot evolved stars were studied by Kochanek (2011), who found that only extremely high mass-loss rates ($\dot{M} > 10^{-2.5}\,M_{\odot}$ yr^{-1}) allowed for efficient condensation while providing sufficient self-shielding from UV radiation. In this context, the supply of gas-phase Si in η Car could be explained by looking at the impact of the fast winds of the central stars on the ejecta from the Great Eruption. In timescales of months/years, several solar masses of processed material were expelled, a fraction of which expanded in the equatorial plane of the system. This matter, dense and hot, eventually cooled down enough to allow for the condensation of dust grains.

The dust content of the Homunculus at different spatial scales has been thoroughly studied by Morris et al. (1999) and Chesneau et al. (2005), who concluded that only a mix of silicates and corundum can account for the spectral features observed in the infrared. This dust has been continuously exposed to the strong, optically thick primary wind ($v_{inf} \sim$ 420 km s^{-1}), plus the intermittent impact of the much faster secondary wind ($v_{inf} \sim 3000$ km s^{-1}) modulated by the orbital cycle. The competing effect of these winds could possibly explain the processing of dust in the inner borders of the butterfly region, releasing Si back to the gas phase (and explaining the radial offset observed between SiO and CO/^{13}CO emission reported in Section 3.2). We could also speculate about the differences in brightness of the SiO clumps resorting to the most accepted orbital geometry (e.g., Teodoro et al. 2016), which places the periastron on the far side of the orbit (i.e., "behind" η Car A, in the S/SE direction, where SiO emission is more intense). This is also the dominant direction where receding, highly compressed fossil wind structures pile up (Gull et al. 2016) as a result of the fast dive of the secondary into the primary wind. The accumulated effect of such abrupt changes in the wind regime over several orbital cycles may favor the dust processing on the far side, hence explaining the observed brightness differences.

Chemical models addressing the formation and destruction of Si-bearing species predict two dominant formation routes for SiO, namely, (1) oxidation of gas-phase Si, primarily through Si + CO → SiO + C and Si + OH → SiO + H (Agúndez & Cernicharo 2006), and (2) reaction with sulfur-bearing compounds via Si + SO → SiO + S and Si + SO_2 → SiO + SO (Zanchet et al. 2018). The detection of CO (Loinard et al. 2012; Smith et al. 2018b) and OH in the Homunculus (Verner et al. 2005; Gull et al. 2020) may suggest that the former reactions are the preferential formation channels of SiO, whereas no other sulfur-bearing species—besides SiS in this work—have ever been reported. In particular, SO_2, one of the main reservoirs of sulfur in AGB stars (Danilovich et al. 2016), has not yet been detected toward η Car. The ALMAGAL setup covers eight transitions of SO_2 spanning a wide range of E_L values (∼200–3000 cm^{-1}), allowing us to set a 3σ upper limit column density $N(SO_2) < 10^{18}$ cm^{-2} following the assumptions in Section 3.3. This value, however, does not really set tight constraints and still allows for a high fractional abundance. Finally, an alternate pathway for SiO formation involves the destruction of SiS through SiS + O → SiO + S. For this reaction to be dominant, sufficient free oxygen has to be available, which is unlikely in the environment of η Car, given that most of it should already be locked in CO and other less abundant species like OH. However, it could explain an overabundance of SiO in the clumps where no SiS is detected.

Regarding SiS, the kinetics of chemical reactions leading to its formation are less understood. The primary paths involve reactions with SO and SO_2, competing with SiO but having lower reaction rate coefficients (Zanchet et al. 2018). As a consequence, the formation rate of SiO is always higher (by a factor of 5–7) than SiS. In a recent work, Mota et al. (2021) proposed an alternate gas-phase reaction, Si + SH → SiS + H, that was able to successfully explain the SiS overabundances observed in L1157 (Podio et al. 2017).

Follow-up observations specifically targeting other sulfur carriers will provide better insight on the feasibility of the different formation routes of SiO and SiS. We note, though, that most of the available chemical models address the conditions and abundances found in circumstellar envelopes or star-forming regions and hence may not be directly applicable to η Car, where conditions may differ by a large margin. The development of ad hoc models will surely be needed to explain the life cycle of Si-bearing species in such a harsh, unusual ambient.

The formation of SiN is probably related to that of SiO and SiS. However, the current understanding of SiN gas-phase chemistry is limited. Provided that shocks supply enough Si, one of the main formation routes for SiN would be the

neutral–neutral reaction (Roveri et al. 1988) Si + NH → SiN + H. In C-rich environments, another possible source of SiN could be a dissociative electron recombination following the reaction $Si^+ + NH_3 \rightarrow SiNH_2^+ + H$ (Turner 1992). In η Car, these two routes seem feasible considering the recent detection of NH and NH_3 (Gull et al. 2020), a significant fraction of which may reside in the equatorial regions where SiN is found. Indeed, the high SiN abundance reflects the unusually nitrogen-rich chemistry of the Homunculus, consistent with heavily processed CNO ejecta.

3.6. Is Maser Emission Possible?

The column densities and abundances derived in Section 3.4 assume a thermal origin for the emission of all molecules. However, masers of SiO and its isotopologues have been frequently observed in envelopes of evolved stars (Schwartz et al. 1982; Pardo et al. 1998; Kim et al. 2010; Rizzo et al. 2021), even in their vibrational ground states ($v = 0$). SiS masers have been detected as well, but only in IRC+10216 (Henkel et al. 1983; Fonfría Expósito et al. 2006). One may wonder whether the maser scenario may also hold in η Car. In fact, SiO and SiS show some features that might be compatible with a maser contribution. First, SiO maser emission in evolved stars is generally clumpy, arising from discrete, very compact regions that usually trace a circumstellar ring due to tangential amplification (Colomer et al. 1992; Diamond et al. 1994, 1997); such a morphology resembles the spatial distribution of SiO around η Car, although at very different angular scales. Second, maser emission tends to show narrower velocity profiles than thermal emission; in our case, we observe that SiO and SiS have significantly narrower lines than ^{13}CO in many of the studied positions, as shown in Figure 5.

The pumping mechanism of SiO masers is not completely established, with radiative and collisional pumping as the most plausible explanations. For these mechanisms to be effective, H_2 densities in excess of $\sim 10^9$ cm^{-3} and kinetic temperatures above 1000 K are required (Elitzur 1992; Bujarrabal 1994). Such stringent physical conditions are typically found at a few stellar radii from the stellar photosphere in the case of AGB stars, hence posing an important drawback for η Car, where material is located ∼5000 au away from the binary. However, at this point, there is no ground for rejecting the possibility that these conditions are locally met in unresolved, hot, and dense pockets of gas. Any further assumption is mere speculation, as we cannot be certain about the nature of the SiO and SiS lines with just a single transition observed. Follow-up interferometric observations of higher J transitions and other vibrational states will elucidate whether the observed emission is entirely thermal or has a weak maser contribution.

4. Summary and Conclusions

We have analyzed ALMA band 6 observations toward η Car with a resolution better than 0.″4. We report the detection of SiO, SiS, and SiN, the first Si- and S-bearing species found in the outskirts of a highly evolved, early-type massive star. The molecules trace a clumpy equatorial ring that surrounds the central binary at a projected separation of ∼2″, presumably dating back to the Great Eruption in the 19th century.

Considering the abrupt changes of the wind regime due to the binary interaction, we propose the continuous processing of dust grains in the inner rim of the butterfly region as the most likely source of the gas-phase silicon needed for the formation of these species. The recent detection of other molecules typically associated with shock-heated gas, like NH_3, CH_3OH, H_2O, or CH^+ (Gull et al. 2020; Morris et al. 2020), even when their exact location in the Homunculus is yet to be pinpointed, may support this interpretation.

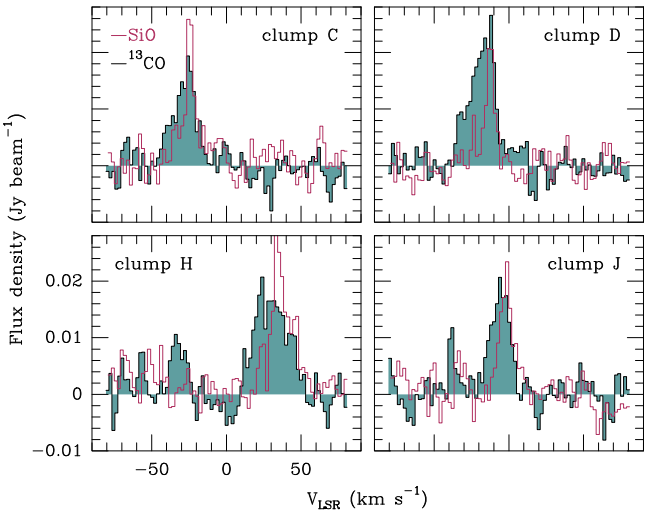

Figure 5. Comparison of the SiO and ^{13}CO line profiles in clumps C, D, H, and J. Spectra have been smoothed to 2 km s^{-1}. All panels have the same intensity scale.

We have derived molecular abundances of $[SiO/H_2] = 6.7 \times 10^{-9}$, $[SiS/H_2] = 1.2 \times 10^{-8}$, and $[SiN/H_2] = 3.6 \times 10^{-8}$ in the clumps. The SiO and SiS abundances are significantly lower than those measured in AGB stars and cool supergiants, (1) making η Car an outstanding object from the perspective of silicon chemistry and (2) further confirming the trend of decreasing SiO and SiS abundances with increasing $\dot{M}$ inferred from observations of AGB stars. We suggest a more efficient readsorption of SiO into dust grains to explain the observed [SiO/SiS] ratio, whereas the prevalence of the rarer SiN over the other Si-bearing compounds seems consistent with the nitrogen-rich nature of the ejecta.

All in all, η Car gives us an unmatched opportunity to examine the life cycle of dust and molecules in the outskirts of a hot, evolved star in affordable timescales. Further and deeper observations to complete its chemical inventory, along with new chemical models able to reproduce its time-dependent conditions, will provide an insightful view of the kinetic networks at work, contributing to filling the gaps in our knowledge about this fascinating object. Finally, we remark that a proper understanding of silicon chemistry in sources like η Car is also crucial to assess the relevance of early-type massive stars as factories of silicate dust, a role so far reserved to cooler objects and supernovae.

We thank Dr. Juan García de la Concepción for the useful discussion about the silicon chemistry. We also thank the anonymous referee for insightful comments that improved the quality and clarity of the paper. The research leading to these results has received funding from the European Commission Horizon 2020 research and innovation program under grant agreement No. 863448 (NEANIAS). J.R.R. acknowledges support by grant PID2019-105552RB-C41 funded by MCIN/AEI/10.13039/501100011033. This paper makes use of the following ALMA data: ADS/JAO.ALMA#2019.1.00195.L.

ALMA is a partnership of ESO (representing its member states), NSF (USA) and NINS (Japan), together with NRC (Canada), MOST and ASIAA (Taiwan), and KASI (Republic of Korea), in cooperation with the Republic of Chile. The Joint ALMA Observatory is operated by ESO, AUI/NRAO and NAOJ.

Data Availability

The data presented in this work are publicly accessible from the ALMA archive. The NEANIAS project fully supports Open Science and encourages the application of FAIR principles. Therefore, we have exported the `MADCUBA` outputs in VO-compliant format (Rizzo et al. 2022) to ensure the interoperability and reproducibility of the modeling results, making them available along with the processed spectra in the Spanish Virtual Observatory Astronomical Data Center at http://svocats.cab.inta-csic.es/etacar_si/. The physical parameters are written as VOTables and the resulting synthetic spectra as verified FITS files[9] compliant with the ObsCore data model.[10]

Appendix A
Full Spectra

Figures 6 and 7 feature the full ALMAGAL spectra toward the 12 clumps indicated in Figure 1.

[9] https://cdsarc.cds.unistra.fr/vizier.submit/fitsvalidator.html
[10] https://www.ivoa.net/documents/ObsCore/

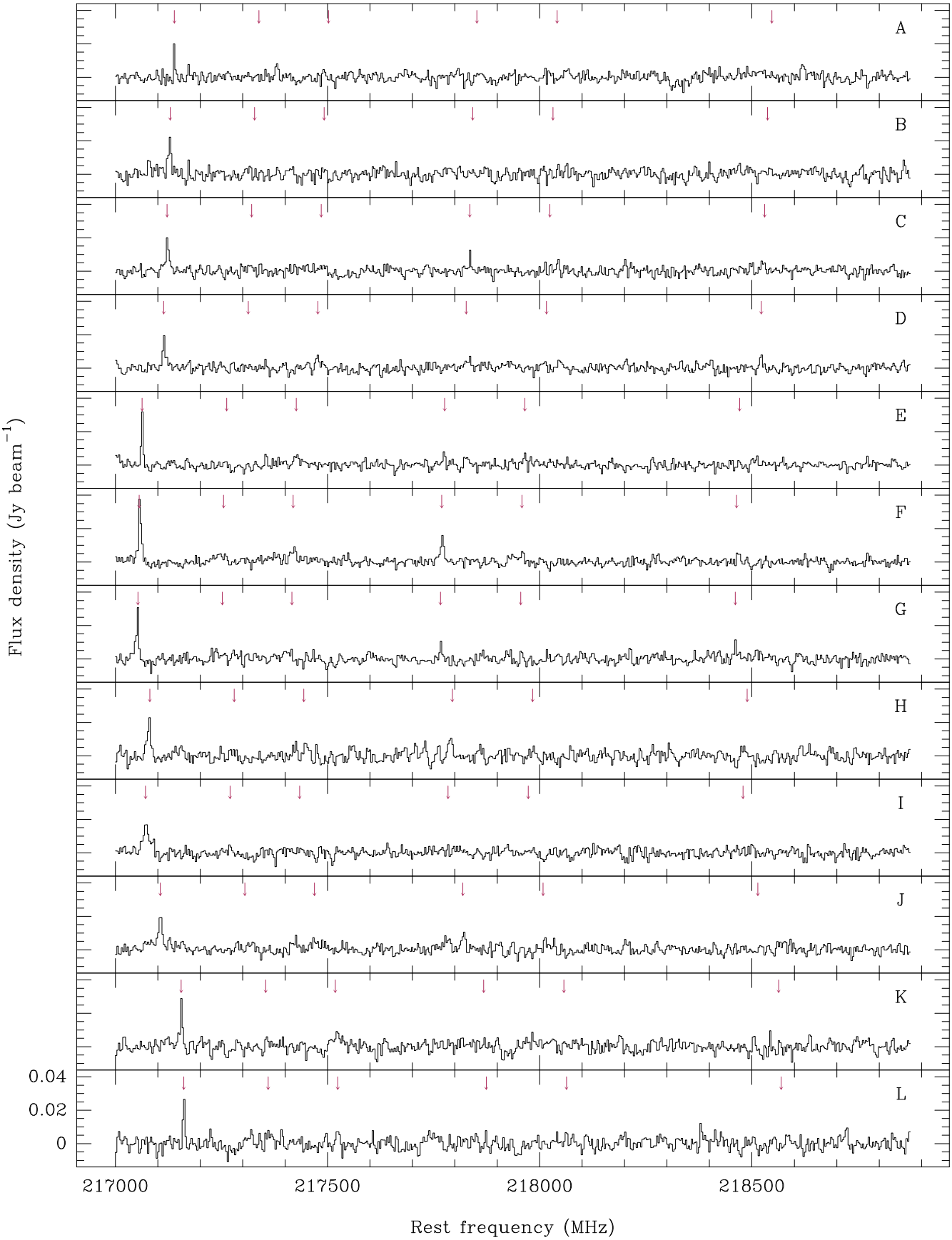

Figure 6. Beam-averaged spectra of η Car between 217.000 and 218.850 GHz extracted from the clumps indicated in Figure 1. The spectra have been smoothed to a resolution of $\sim$5 km s^{-1}. In each panel, the markers indicate the frequencies of the transitions listed in Table 1 shifted to the velocity of the strongest SiO component.

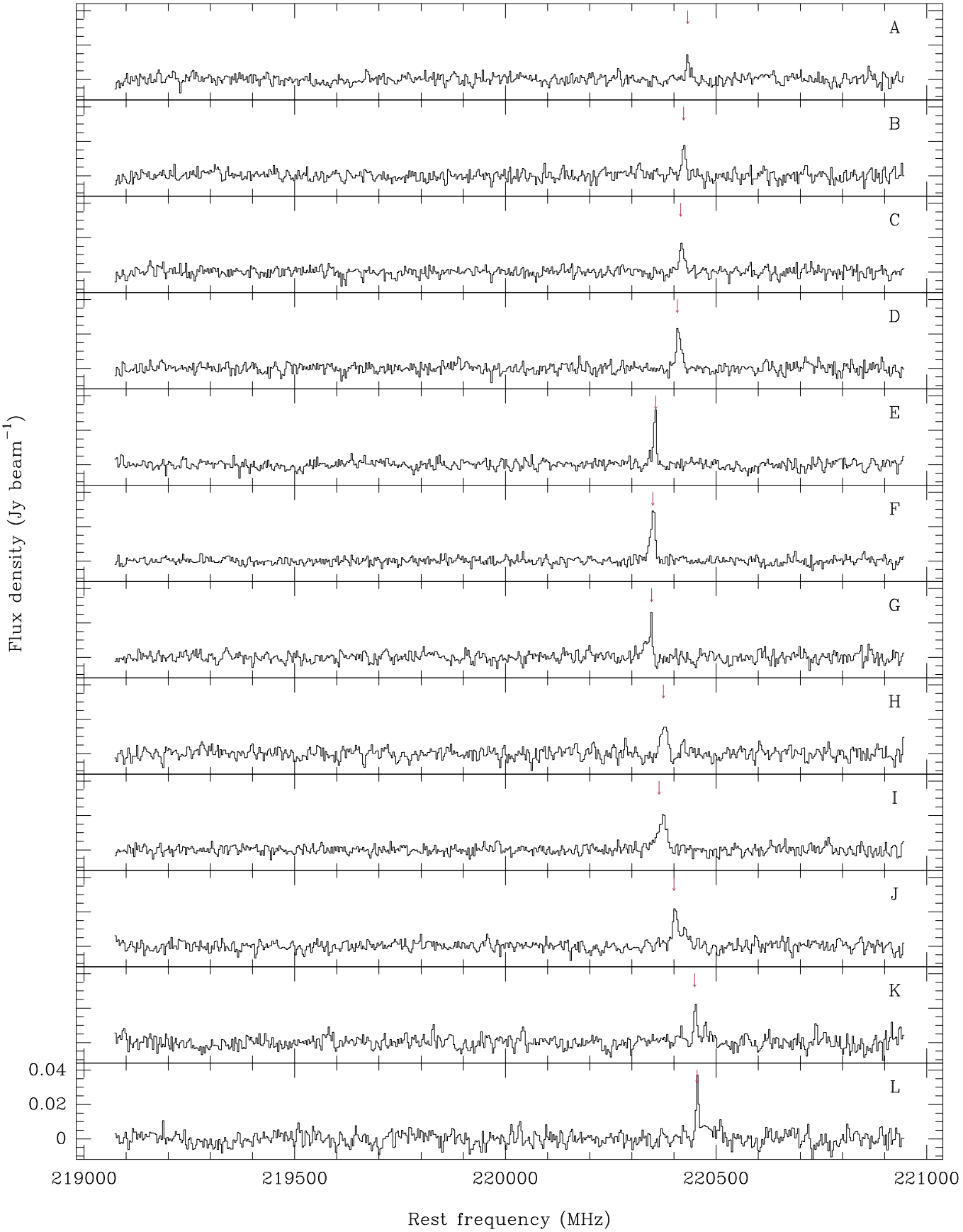

Figure 7. Beam-averaged spectra of η Car between 219.100 and 220.950 GHz extracted from the clumps indicated in Figure 1. The spectra have been smoothed to a resolution of $\sim$5 km s^{-1}. In each panel, the markers indicate the frequency of the ^{13}CO $J = 2 \rightarrow 1$ transition shifted to the velocity of the strongest SiO component.

Appendix B
Line Fitting

Tables 3 and 4 list the MADCUBA line fitting parameters for all the components detected with an S/N above 3σ.

Table 3
MADCUBA Line Fitting Parameters for SiO, SiS, and SiN

Pos.	$(\Delta\alpha, \Delta\delta)$	T_{ex} (K)	No.	SiO			SiS			SiN		
				v_{LSR} (km s^{-1})	Δv (km s^{-1})	$\int T_{mb}\delta v$ (K km s^{-1})	v_{LSR} (km s^{-1})	Δv (km s^{-1})	$\int T_{mb}\delta v$ (K km s^{-1})	v_{LSR} (km s^{-1})	Δv (km s^{-1})	$\int T_{mb}\delta v$ (K km s^{-1})
A	(+0.9, +2.6)	154	1	−47.4	3.9 (0.4)	25.11 (2.43)	⋯	⋯	⋯	⋯	⋯	⋯
B	(+1.2, +2.2)	166	1	−33.5	5.4 (0.7)	34.16 (2.62)	⋯	⋯	⋯	⋯	⋯	⋯
			2	−25.4	7.1 (1.7)	15.09 (2.99)	⋯	⋯	⋯	⋯	⋯	⋯
C	(+0.9, +1.9)	180	1	−24.3	6.7 (0.6)	42.52 (3.33)	−24.9	4.4 (0.3)	17.36 (0.88)	⋯	⋯	⋯
D	(+1.2, +1.7)	185	1	−23.5	2.5 (0.4)	6.17 (0.91)	−24.4	5.5 (0.7)	10.72 (1.13)	⋯	⋯	⋯
			2	−12.4	6.4 (0.3)	34.66 (1.47)	−12.4	2.7 (0.4)	5.89 (0.79)	−14.3	4.2 (3.8)	3.88 (1.45)
E	(+2.0, +0.4)	179	1	57.8	5.9 (0.2)	53.86 (1.40)	58.0	8.6 (1.2)	26.13 (3.19)	⋯	⋯	⋯
F	(+2.0, −0.2)	173	1	59.2	4.8 (0.9)	19.35 (2.04)	60.0	6.0 (1.9)	14.49 (2.30)	56.6	10.0 (4.3)	5.84 (2.70)
			2	65.9	5.7 (0.4)	65.46 (2.21)	65.8	5.0 (1.0)	23.58 (2.11)	64.7	4.9 (2.0)	4.19 (1.88)
G	(+1.8, −0.9)	163	1	71.2	4.7 (0.5)	37.83 (1.98)	69.3	7.7 (0.6)	27.63 (1.99)	70.1	2.9 (0.8)	4.51 (1.32)
			2	78.4	13.7 (2.5)	43.98 (3.37)	⋯	⋯	⋯	⋯	⋯	⋯
H	(+0.5, −1.1)	211	1	23.6	3.8 (0.7)	9.94 (1.44)	⋯	⋯	⋯	⋯	⋯	⋯
			2	34.3	7.3 (0.6)	52.68 (2.00)	33.7	5.9 (1.0)	22.04 (1.65)	⋯	⋯	⋯
			3	40.4	2.9 (1.2)	7.08 (1.25)	39.5	4.0 (1.0)	12.94 (1.36)	⋯	⋯	…[a]
			4	45.9	6.3 (1.0)	23.08 (1.86)	44.9	5.0 (1.0)	14.05 (1.51)	⋯	⋯	⋯
	(−0.3, −2.2)	165	1	44.0	31.0 (2.5)	82.44 (5.44)	⋯	⋯	⋯	⋯	⋯	⋯
			2	45.5	3.2 (1.8)	11.71 (1.75)	⋯	⋯	⋯	⋯	⋯	⋯
J	(−1.3, −2.3)	162	1	−5.7	5.8 (0.9)	16.68 (2.47)	−5.2	11.3 (1.4)	29.25 (2.76)	⋯	⋯	⋯
			2	−0.6	5.0 (1.0)	27.05 (2.29)	⋯	⋯	⋯	⋯	⋯	⋯
K	(−2.3, −1.1)	168	1	−76.1	2.5 (0.7)	4.96 (1.05)	⋯	⋯	⋯	⋯	⋯	⋯
			2	−70.0	5.5 (0.3)	45.99 (1.57)	⋯	⋯	⋯	⋯	⋯	⋯
			3	−61.0	5.3 (0.8)	13.75 (1.54)	⋯	⋯	⋯	⋯	⋯	⋯
L	(−2.0, −0.5)	180	1	−78.1	5.7 (0.3)	49.68 (2.20)	−76.5	3.5 (0.6)	10.03 (1.52)	⋯	⋯	⋯

Notes. The fourth column gives the component number in order of increasing velocity. The fitting of SiN only considers the component at 218.512 GHz.
[a] Tentative detection at 2.5σ (see text).

Table 4
MADCUBA Line Fitting Parameters for ^{13}CO and ^{13}CN

Pos.	$(\Delta\alpha, \Delta\delta)$	T_{ex} (K)	No.	^{13}CO			^{13}CN		
				v_{LSR} (km s^{-1})	Δv (km s^{-1})	$\int T_{mb}\delta v$ (K km s^{-1})	v_{LSR} (km s^{-1})	Δv (km s^{-1})	$\int T_{mb}\delta v$ (K km s^{-1})
A	(+0.9, +2.6)	154	1	−46.4	9.2 (1.0)	33.74 (3.21)	⋯	⋯	⋯
B	(+1.2, +2.2)	166	1	−43.0	2.7 (0.7)	5.98 (1.10)	⋯	⋯	⋯
			2	−38.4	3.4 (1.3)	6.74 (1.23)	⋯	⋯	⋯
			3	−33.3	8.8 (2.9)	38.02 (1.98)	⋯	⋯	⋯
			4	−23.8	3.7 (3.9)	3.84 (1.29)	⋯	⋯	⋯
C	(+0.9, +1.9)	180	1	−33.4	4.9 (0.0)[a]	11.13 (2.65)	⋯	⋯	⋯
			2	−25.2	10.9 (0.9)	46.22 (3.24)	⋯	⋯	⋯
D	(+1.2, +1.7)	185	1	−32.8	4.1 (1.1)	6.63 (1.75)	⋯	⋯	⋯
			2	−16.6	18.5 (0.8)	101.84 (3.72)	−12.8	13.5 (3.1)	0.01 (1.67)
E	(+2.0, +0.4)	179	1	57.9	6.1 (0.2)	51.37 (1.74)	58.2	13.5 (3.2)	0.01 (1.46)
			2	63.9	6.7 (0.8)	23.88 (2.43)	⋯	⋯	⋯
F	(+2.0, −0.2)	173	1	56.4	1.1 (0.9)	0.77 (0.40)	⋯	⋯	⋯
			2	64.5	11.4 (0.3)	91.38 (2.03)	62.3	10.4 (2.0)	0.01 (1.41)
			3	73.5	2.4 (0.0)[a]	7.89 (3.43)	⋯	⋯	⋯
			4	80.4	2.4 (0.0)[a]	7.33 (3.39)	⋯	⋯	⋯
G	(+1.8, −0.9)	163	1	71.1	5.6 (0.4)	38.45 (1.60)	⋯	⋯	⋯
			2	79.8	8.9 (4.7)	16.83 (2.01)	⋯	⋯	⋯
			3	91.9	13.0 (3.1)	26.09 (2.42)	⋯	⋯	⋯
H	(+0.5, −1.1)	211	1	12.2	1.8 (0.2)	3.84 (0.41)	⋯	⋯	⋯
			2	21.7	9.6 (0.7)	34.49 (2.31)	25.3	12.5 (6.1)	0.01 (2.16)
			3	31.7	7.8 (1.5)	10.68 (1.92)	⋯	⋯	⋯

Table 4
(Continued)

Pos.	$(\Delta\alpha, \Delta\delta)$	T_{ex} (K)	No.	^{13}CO v_{LSR} (km s^{-1})	^{13}CO Δv (km s^{-1})	^{13}CO $\int T_{mb}\delta v$ (K km s^{-1})	^{13}CN v_{LSR} (km s^{-1})	^{13}CN Δv (km s^{-1})	^{13}CN $\int T_{mb}\delta v$ (K km s^{-1})
			4	35.4	18.6 (1.4)	52.00 (3.36)	⋯	⋯	⋯
			5	44.7	4.3 (0.9)	6.18 (1.20)	⋯	⋯	⋯
I	(−0.3, −2.2)	165	1	19.3	6.5 (0.8)	17.61 (1.78)	⋯	⋯	⋯
			2	29.9	10.1 (0.6)	43.72 (2.29)	⋯	⋯	⋯
			3	40.3	18.3 (1.4)	44.90 (3.05)	⋯	⋯	⋯
			4	52.4	29.3 (4.1)	29.74 (3.79)	⋯	⋯	⋯
			5	70.0	47.0 (9.3)	23.84 (5.04)	⋯	⋯	⋯
J	(−1.3, −2.3)	162	1	−37.9	5.8 (0.0)[a]	25.12 (2.50)	⋯	⋯	⋯
			2	−6.7	24.7 (1.2)	124.21 (5.17)	⋯	⋯	⋯
K	(−2.3, −1.1)	168	1	−121.0	4.9 (0.8)	10.06 (1.44)	⋯	⋯	⋯
			2	−103.7	7.7 (0.6)	26.15 (1.80)	⋯	⋯	⋯
			3	−71.5	10.2 (0.4)	58.91 (2.07)	−76.4	14.1 (2.5)	0.02 (2.31)
			4	−26.5	5.6 (0.7)	13.96 (1.54)	⋯	⋯	⋯
L	(−2.0, −0.5)	180	1	−154.1	3.8 (0.5)	16.61 (1.76)	⋯	⋯	⋯
			2	−78.0	8.8 (0.3)	78.93 (2.68)	−79.3	13.3 (3.2)	0.02 (2.39)

Notes. The fourth column gives the component number in order of increasing velocity.
[a] The parameter had to be fixed to allow the fitting to converge simultaneously for all components.

ORCID iDs

C. Bordiu https://orcid.org/0000-0002-7703-0692
J. R. Rizzo https://orcid.org/0000-0002-8443-6631
F. Bufano https://orcid.org/0000-0002-3429-2481
G. Quintana-Lacaci https://orcid.org/0000-0002-5417-1943
C. Buemi https://orcid.org/0000-0002-7288-4613
P. Leto https://orcid.org/0000-0003-4864-2806
F. Cavallaro https://orcid.org/0000-0003-1856-6806
L. Cerrigone https://orcid.org/0000-0002-5537-7134
A. Ingallinera https://orcid.org/0000-0002-3137-473X
S. Loru https://orcid.org/0000-0001-5126-1719
S. Riggi https://orcid.org/0000-0001-6368-8330
C. Trigilio https://orcid.org/0000-0002-1216-7831
G. Umana https://orcid.org/0000-0002-6972-8388
E. Sciacca https://orcid.org/0000-0002-5574-2787

References

Abraham, Z., Beaklini, P. P. B., Cox, P., Falceta-Gonçalves, D., & Nyman, L. Å. 2022, MNRAS, 517, 47
Agúndez, M., & Cernicharo, J. 2006, ApJ, 650, 374
Asplund, M., Amarsi, A. M., & Grevesse, N. 2021, ApJ, 653, A141
Bordiu, C., & Rizzo, J. R. 2019, MNRAS, 490, 1570
Bujarrabal, V. 1994, A&A, 285, 953
Bujarrabal, V., Fuente, A., & Omont, A. 1994, A&A, 285, 247
Caselli, P., Hartquist, T. W., & Havnes, O. 1997, A&A, 322, 296
Chesneau, O., Min, M., Herbst, T., et al. 2005, A&A, 435, 1043
Colomer, F., Graham, D. A., Krichbaum, T. P., et al. 1992, A&A, 254, L17
Damineli, A. 1996, ApJL, 460, L49
Damineli, A., Hillier, D. J., Corcoran, M. F., et al. 2008, MNRAS, 384, 1649
Danilovich, T., De Beck, E., Black, J. H., Olofsson, H., & Justtanont, K. 2016, A&A, 588, A119
Danilovich, T., Ramstedt, S., Gobrecht, D., et al. 2018, A&A, 617, A132
Danilovich, T., Richards, A. M. S., Karakas, A. I., et al. 2019, MNRAS, 484, 494
Davidson, K., Dufour, R. J., Walborn, N. R., & Gull, T. R. 1986, ApJ, 305, 867
Davidson, K., & Humphreys, R. 2012, Eta Carinae and the Supernova Impostors (New York: Springer)
Davidson, K., Walborn, N. R., & Gull, T. R. 1982, ApJL, 254, L47
De Beck, E., & Olofsson, H. 2020, A&A, 642, A20
Diamond, P. J., Kemball, A. J., & Boboltz, D. A. 1997, VA, 41, 175
Diamond, P. J., Kemball, A. J., Junor, W., et al. 1994, ApJL, 430, L61
Dickinson, D. F., & Kuiper, E. N. R. 1981, ApJ, 247, 112
Dufour, R. J., Glover, T. W., Hester, J. J., et al. 1997, in ASP Conf. Ser. 120, Luminous Blue Variables: Massive Stars in Transition, ed. A. Nota & H. Lamers (San Francisco, CA: ASP), 255
Elitzur, M. 1992, Astronomical Masers, Vol. 170 (Dordrecht: Kluwer)
Fonfría Expósito, J. P., Agúndez, M., Tercero, B., Pardo, J. R., & Cernicharo, J. 2006, ApJL, 646, L127
Frew, D. J. 2004, JAD, 10, 6
Gaviola, E. 1950, ApJ, 111, 408
González Delgado, D., Olofsson, H., Kerschbaum, F., et al. 2003, A&A, 411, 123
Grasshoff, M., Tiemann, E., & Henkel, C. 1981, A&A, 101, 238
Guillet, V., Jones, A. P., & Pineau des Forêts, G. 2009, A&A, 497, 145
Guillet, V., Pineau des Forets, G., & Jones, A. P. 2011, A&A, 527, A123
Gull, T. R., Madura, T. I., Teodoro, M., et al. 2016, MNRAS, 462, 3196
Gull, T. R., Morris, P. W., Black, J. H., et al. 2020, MNRAS, 499, 5269
Gull, T. R., Nielsen, K. E., Corcoran, M. F., et al. 2009, MNRAS, 396, 1308
Gusdorf, A., Cabrit, S., Flower, D. R., & Pineau des Forets, G. 2008, A&A, 482, 809
Henkel, C., Matthews, H. E., & Morris, M. 1983, ApJ, 267, 184
Hillier, D. J., & Allen, D. A. 1992, A&A, 262, 153
Hillier, D. J., Davidson, K., Ishibashi, K., & Gull, T. 2001, ApJ, 553, 837
Iping, R. C., Sonneborn, G., Gull, T. R., Massa, D. L., & Hillier, D. J. 2005, ApJL, 633, L37
Ishibashi, K., Gull, T. R., Davidson, K., et al. 2003, AJ, 125, 3222
Jiménez-Serra, I., Martín-Pintado, J., Rodríguez-Franco, A., & Marcelino, N. 2004, ApJL, 603, L49
Kim, J., Cho, S.-H., Oh, C. S., & Byun, D.-Y. 2010, ApJS, 188, 209
Kochanek, C. S. 2011, ApJ, 743, 73
Kraus, M., Oksala, M. E., Cidale, L. S., et al. 2015, ApJL, 800, L20
Lefloch, B., Castets, A., Cernicharo, J., & Loinard, L. 1998, ApJL, 504, L109
Levenberg, K. 1944, QApMa, 2, 164
Loinard, L., Kamiński, T., Serra, P., et al. 2016, ApJ, 833, 48
Loinard, L., Menten, K. M., Güsten, R., Zapata, L. A., & Rodríguez, L. F. 2012, ApJL, 749, L4
Lucas, R., Bujarrabal, V., Guilloteau, S., et al. 1992, A&A, 262, 491
Marquardt, D. W. 1963, SJAM, 11, 431
Martín, S., Martín-Pintado, J., Blanco-Sánchez, C., et al. 2019, A&A, 631, A159
Martin-Pintado, J., Bachiller, R., & Fuente, A. 1992, A&A, 254, 315
Massalkhi, S., Agúndez, M., & Cernicharo, J. 2019, A&A, 628, A62
Massalkhi, S., Agúndez, M., Cernicharo, J., & Velilla-Prieto, L. 2020, A&A, 641, A57
Morris, M., Redman, R., Reid, M. J., & Dickinson, D. F. 1979, ApJ, 229, 257
Morris, P. W., Charnley, S. B., Corcoran, M., et al. 2020, ApJL, 892, L23

Morris, P. W., Gull, T. R., Hillier, D. J., et al. 2017, ApJ, 842, 79
Morris, P. W., Waters, L. B. F. M., Barlow, M. J., et al. 1999, Natur, 402, 502
Mota, V. C., Varandas, A. J. C., Mendoza, E., Wakelam, V., & Galvao, B. R. L. 2021, ApJ, 920, 37
Okazaki, A. T., Owocki, S. P., Russell, C. M. P., & Corcoran, M. F. 2008, MNRAS, 388, L39
Pardo, J. R., Cernicharo, J., Gonzalez-Alfonso, E., & Bujarrabal, V. 1998, A&A, 329, 219
Podio, L., Codella, C., Lefloch, B., et al. 2017, MNRAS, 470, L16
Quintana-Lacaci, G., Agúndez, M., Cernicharo, J., et al. 2016, A&A, 592, A51
Ramstedt, S., Schöier, F. L., & Olofsson, H. 2009, A&A, 499, 515
Rizzo, J. R., Blanco, C., & Martin-Pintado, J. 2022, VIOMASS: Virtual Observatory Integration Of Madcuba And SLIM Spectra, v1.0, Zenodo, doi:10.5281/zenodo.7046117
Rizzo, J. R., Cernicharo, J., & García-Miró, C. 2021, ApJS, 253, 44
Rizzo, J. R., Palau, A., Jiménez-Esteban, F., & Henkel, C. 2014, A&A, 564, A21
Roveri, R. M., Erdelyi Mendes, M., & Singh, P. D. 1988, A&A, 199, 127
Schilke, P., Leurini, S., Menten, K. M., & Alcolea, J. 2003, A&A, 412, L15
Schilke, P., Walmsley, C. M., Pineau des Forets, G., & Flower, D. R. 1997, A&A, 321, 293
Schöier, F. L., Bast, J., Olofsson, H., & Lindqvist, M. 2007, A&A, 473, 871
Schöier, F. L., Olofsson, H., & Lundgren, A. A. 2006, A&A, 454, 247
Schwartz, P. R., Zuckerman, B., & Bologna, J. M. 1982, ApJL, 256, L55
Singh, A. P., Edwards, J. L., Humphreys, R. M., & Ziurys, L. M. 2021, ApJL, 920, L38
Smith, N. 2004, MNRAS, 351, L15
Smith, N. 2006, ApJ, 644, 1151
Smith, N. 2013, MNRAS, 429, 2366
Smith, N., Andrews, J. E., Rest, A., et al. 2018a, MNRAS, 480, 1466
Smith, N., Brooks, K. J., Koribalski, B. S., & Bally, J. 2006, ApJL, 645, L41
Smith, N., & Davidson, K. 2001, ApJL, 551, L101
Smith, N., & Frew, D. J. 2011, MNRAS, 415, 2009
Smith, N., Gehrz, R. D., Hinz, P. M., et al. 2003, AJ, 125, 1458
Smith, N., Ginsburg, A., & Bally, J. 2018b, MNRAS, 474, 4988
Smith, N., & Morse, J. A. 2004, ApJ, 605, 854
Smith, N., & Morse, J. A. 2019, MNRAS, 489, 268
Smith, N., Morse, J. A., Gull, T. R., et al. 2004, ApJ, 605, 405
Sobolev, V. V. 1960, Moving Envelopes of Stars (Cambridge: Harvard Univ. Press)
Teodoro, M., Damineli, A., Heathcote, B., et al. 2016, ApJ, 819, 131
Turner, B. E. 1992, ApJL, 388, L35
van der Tak, F. F. S., Black, J. H., Schöier, F. L., Jansen, D. J., & van Dishoeck, E. F. 2007, A&A, 468, 627
Verner, E., Bruhweiler, F., Nielsen, K. E., et al. 2005, ApJ, 629, 1034
Wilson, R. W., Penzias, A. A., Jefferts, K. B., Kutner, M., & Thaddeus, P. 1971, ApJL, 167, L97
Wong, K. T., Kamiński, T., Menten, K. M., & Wyrowski, F. 2016, A&A, 590, A127
Zanchet, A., Roncero, O., Agúndez, M., & Cernicharo, J. 2018, ApJ, 862, 38
Zapata, L. A., Loinard, L., Fernández-López, M., et al. 2022, ApJ, 935, 76
Ziurys, L. M. 1988, ApJ, 324, 544
Ziurys, L. M., Milam, S. N., Apponi, A. J., & Woolf, N. J. 2007, Natur, 447, 1094